Express Polymer Letters Vol.16, No.2 (2022) 130–141
Available online at www.expresspolymlett.com
https://doi.org/10.3144/expresspolymlett.2022.11

Research article

Effective strain criterion under multimode and multiaxial loadings – A rubber S–N curve with the scatter-band factor of 1.6 from 90 fatigue cases

*Robert Keqi Luo**

Trelleborg Antivibration Solutions, Leicester LE4 2BN, UK

Received 19 June 2021; accepted in revised form 17 September 2021

Abstract. The effective strain criterion, unifying multimode and multiaxial loadings to a single parameter and being expressed in analytical form with no need to rotate a plane to search the maximum damage parameter, is proposed for the fatigue design of anti-vibration components. The validation procedure was performed on 90 cases in two aspects: fatigue damage and crack orientation. All predicted fatigue cracks were located at the places where the effective strain reached its maximum and was consistent with the experimental observations. The failure planes predicted correlated with the experimental measurement. The S–N curve covered over 10^2 to $2.4 \cdot 10^6$ cycles and achieved high accuracy with the scatter-band of 1.8. The proposed approach was applied to two non-proportional loading cases (one in a phase angle 45° and the other in a phase angle 90°). The results seemed to indicate the suitability of the approach for the non-proportional loading calculations. It would be possible to combine the proposed approach with the critical plane method in non-proportional loadings: using the proposed approach to find the critical loading range and then using the critical plane method to determine the maximum values of the required damage variables. Both the proposed concept and the obtained S–N curve would be beneficial in rubber fatigue design. More engineering cases may be needed to verify this approach further.

Keywords: *rubber fatigue, failure criteria, effective strain, modeling and simulation, antivibration design*

1. Introduction

An effective criterion is a key requirement at a stage of fatigue design of rubber anti-vibration products in the industry. Many researchers have developed different fatigue damage criteria with certain levels of success. Bourchak and Aid [1] employed both the maximum stress criterion and the strain energy density criterion to estimate the fatigue damage of the polymer pipes. Their comparison showed different results between the two criteria. Verron [2] proposed a criterion using the minimum configurational stress, and this concept was adopted by le Cam *et al.* [3] to evaluate fatigue damage. Luo and coworkers [4, 5] developed the effect stress idea, and several researchers applied it to a number of industrial products [6–9]. Saintier *et al.* [10] employed the equivalent stress to calculate fatigue damage. Mars and coworkers [11–13], Xu *et al.* [14] and Zarrin-Ghalami *et al.* [15] used CED (Cracking Energy Density) to assess the fatigue life of rubber components. Strain-based failure criteria were utilised for fatigue prediction by Zerrin-Ghalami and Fatemi [16], Belkhiria *et al.* [17] and Zarrin-Ghalami [18]. Shangguan and coworkers [19, 20] compared several damage criteria to an industrial rubber product and found that stress-based parameters achieved higher accuracy than strain-based and energy-based ones. Nyaaba *et al.* [21], Zarrin-Ghalami *et al.* [15], Chung and Kim [22], Lu *et al.* [23], used the critical plane method to obtain the maximum damage from their criteria. This searching

*Corresponding author, e-mail: robert.luo@trelleborg.com
© BME-PT

approach is effective in a proportional loading case. However, there are much more complex issues in a non-proportional loading case. To find the maximum damage value in a non-proportional loading event, a calculation procedure needs to be performed at different loading proportions with varying bases, which may involve a significant additional amount of calculation.

In this article, an effective strain criterion, unifying multimode and multiaxial loadings to a single parameter and being expressed in analytical forms with no need to rotate a plane to search the maximum damage parameter, is proposed for fatigue design of anti-vibration products in the industry. In addition, this could be combined with the critical plane method so that substantial CPU time could be saved. Unlike the effective stress criterion, this proposed criterion is based on strain. Compared with stress, strain can be measured so that the comparison between the experiments and the design simulation can be performed directly in real engineering applications. The remainder of this article is organised in the following order: the effective strain criterion is introduced, followed by a discussion on the type of ring specimen and its finite element models. All findings are summarised after prediction and validation on 90 published fatigue cases in both proportional and non-proportional loading conditions are presented.

2. Effective strain criterion

We consider the following conditions: a cyclic loading is running between state 1 (strain $\boldsymbol{\varepsilon_1}$) and state 2 (strain $\boldsymbol{\varepsilon_2}$), its strain increment is $\Delta\boldsymbol{\varepsilon} = \boldsymbol{\varepsilon_2} - \boldsymbol{\varepsilon_1}$. To calculate the fatigue damage, we need to consider both the increment $\Delta\boldsymbol{\varepsilon}$ and the current strain $\boldsymbol{\varepsilon_2}$. Based on engineering principles and applications, a damage parameter called effective strain $\boldsymbol{\varepsilon_f}$,was developed. It is hypothesised that crack initiation occurs at a position where $\boldsymbol{\varepsilon_f}$ reaches its maximum value during fatigue loading. To be applicable for multimode and multiaxial loading conditions, the criterion includes its principal components ε_{fi} (i = 1, 2, 3) (Equation (1)):

$$\varepsilon_f = \sqrt{\varepsilon_{f1}^2 + A_1\varepsilon_{f2}^2 + A_2\varepsilon_{f3}^2}, \quad \varepsilon_{f1} \geq \varepsilon_{f2} \geq \varepsilon_{f3} \qquad (1)$$

where A_1 and A_2 are weighting functions.

The geometrical meaning of Equation (1) is an ellipsoidal failure envelope, illustrated in Figure 1.

In engineering applications, a higher strain generates more damage than a lower strain does. An S–N curve

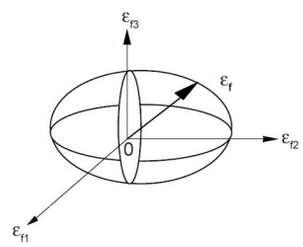

Figure 1. Geometrical illustration of Equation (1).

is a typical case where a higher cyclic number is corresponding to a lower strain and a lower cyclic number is corresponding to a higher strain. Hence, the contribution to fatigue damage from ε_{f2} (ε_{f3}) is less or equal to the contribution from ε_{f1}. For safety, both A_1 and A_2 are taken as integer 1 to maximise the effective strain and the fatigue damage. Therefore, Equation (1) becomes Equation (2):

$$\varepsilon_f = \sqrt{\varepsilon_{f1}^2 + \varepsilon_{f2}^2 + \varepsilon_{f3}^2} \qquad (2)$$

If ε_{f1}, ε_{f2} and ε_{f3} are positive, for a given $\boldsymbol{\varepsilon_f}$, Equation (2) describes a spherical envelope in the first quadrant of a rectangular coordinate system, as illustrated in Figure 2. Any point located on the surface generates the same fatigue damage. When using ε_{f1} only, Equation (2) is simplified to a form of the maximum strain criterion (Equation (3)):

$$\varepsilon_f = \varepsilon_{f1} \qquad (3)$$

From the above description, ε_f needs to be obtained from its three principal components ε_{f1}, ε_{f2} and ε_{f3}. To obtain the principal components of the effective strain $\boldsymbol{\varepsilon_{fi}}$ (i = 1, 2, 3), we denote $\Delta\boldsymbol{\varepsilon_i}$ (i =1, 2, 3) as three principal components of the increment $\Delta\boldsymbol{\varepsilon}$ and the direction of $\boldsymbol{\varepsilon_{fi}}$ is along the same direction of $\Delta\boldsymbol{\varepsilon_i}$. The current strain $\boldsymbol{\varepsilon_2}$ is projected to $\Delta\boldsymbol{\varepsilon_i}$ for $\boldsymbol{\varepsilon_{fi}}$ calculation, as shown in Figure 3. If a projection of $\boldsymbol{\varepsilon_2}$ on $\Delta\boldsymbol{\varepsilon_i}$ is $\boldsymbol{\varepsilon_{2i}}$, two conditions need to be checked for obtaining the magnitude of $\boldsymbol{\varepsilon_{fi}}$. Firstly, both $\Delta\boldsymbol{\varepsilon_i}$ and $\boldsymbol{\varepsilon_{2i}}$ should be in tension, in other words, fatigue damage may not be generated if a point is entirely in compression

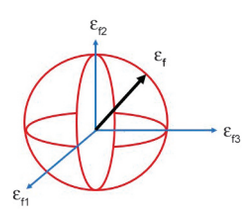

Figure 2. Geometrical illustration of the effective strain Equation (2), (valid on $\varepsilon_{fi} > 0$).

during cyclic loading in anti-vibration applications. This hypothesis can be justified as follows:
Rubber is a type of incompressible, or nearly incompressible, material. Based on the principle of the anti-vibration design, a reasonable free space needs to be designed through which it may flow, providing the required stiffness and energy absorption. Industrial anti-vibration research on fatigue damage in a completely compressive zone, as opposed to other locations, was not found during a limited literature search. Some researchers, *e.g.*, Saintier *et al.* [10] indicated that compressive stresses had no effect on fatigue lifetime in the stress ranges that they considered.
Secondly, $\Delta\boldsymbol{\varepsilon}_{\mathbf{i}}$ and $\boldsymbol{\varepsilon}_{\mathbf{2i}}$ should be compared to calculate $\varepsilon_{\mathrm{fi}}$. For contribution to fatigue damage from $\boldsymbol{\varepsilon}_{\mathbf{fi}}$, the compression portion of $\boldsymbol{\varepsilon}_{\mathbf{fi}}$ should not be greater than the tension portion of $\boldsymbol{\varepsilon}_{\mathbf{fi}}$. Hence, the magnitude of $\boldsymbol{\varepsilon}_{\mathbf{fi}}$ can be calculated based on the Equations (4), (5):

$$\varepsilon_{\mathrm{fi}} = \Delta\varepsilon_{\mathrm{i}}, \ \text{if} \ \ 2\varepsilon_{2\mathrm{i}} \geq \Delta\varepsilon_{\mathrm{i}} \tag{4}$$

$$\varepsilon_{\mathrm{fi}} = 2\varepsilon_{2\mathrm{i}}, \ \text{if} \ \ 2\varepsilon_{2\mathrm{i}} < \Delta\varepsilon_{\mathrm{i}} \tag{5}$$

If the current strain $\varepsilon_{2\mathrm{i}} = 0.2$ and the increment strain $\Delta\varepsilon_{\mathrm{i}} = 0.5$, $\varepsilon_{\mathrm{fi}} = 0.4$ (from Equation (5)). If the current strain $\varepsilon_{2\mathrm{i}} = 0.3$ and the increment strain $\Delta\varepsilon_{\mathrm{i}} = 0.5$, $\varepsilon_{\mathrm{fi}} = 0.5$ (from Equation (4)).
The direction of the effective strain $\boldsymbol{\varepsilon}_{\mathbf{f}}$ determines a failure plane of a fatigue crack.
Let projections of $\boldsymbol{\varepsilon}_{\mathbf{fi}}$ to three axes of a coordinate system be Equation (6):

$$\begin{aligned} \boldsymbol{\varepsilon}_{\mathbf{f1}} &= \left[\varepsilon_{\mathrm{f}1i}, \varepsilon_{\mathrm{f}1j}, \varepsilon_{\mathrm{f}1k}\right] \\ \boldsymbol{\varepsilon}_{\mathbf{f2}} &= \left[\varepsilon_{\mathrm{f}2i}, \varepsilon_{\mathrm{f}2j}, \varepsilon_{\mathrm{f}2k}\right] \\ \boldsymbol{\varepsilon}_{\mathbf{f3}} &= \left[\varepsilon_{\mathrm{f}3i}, \varepsilon_{\mathrm{f}3j}, \varepsilon_{\mathrm{f}3k}\right] \end{aligned} \tag{6}$$

Then the direction is Equation (7)–(10):

$$\mathbf{d} = \left[d_i, d_j, d_k\right] \tag{7}$$

$$d_i = \frac{\varepsilon_{\mathrm{f}1i} + \varepsilon_{\mathrm{f}1i} + \varepsilon_{\mathrm{f}1i}}{M} \tag{8}$$

$$d_j = \frac{\varepsilon_{\mathrm{f}1j} + \varepsilon_{\mathrm{f}1j} + \varepsilon_{\mathrm{f}1j}}{M} \tag{9}$$

$$d_k = \frac{\varepsilon_{\mathrm{f}1k} + \varepsilon_{\mathrm{f}1k} + \varepsilon_{\mathrm{f}1k}}{M} \tag{10}$$

where (Equation (11)):

$$M = \sqrt{(\varepsilon_{\mathrm{f}1i} + \varepsilon_{\mathrm{f}2i} + \varepsilon_{\mathrm{f}3i})^2 + (\varepsilon_{\mathrm{f}1j} + \varepsilon_{\mathrm{f}2j} + \varepsilon_{\mathrm{f}3j})^2 + (\varepsilon_{\mathrm{f}1k} + \varepsilon_{\mathrm{f}2k} + \varepsilon_{\mathrm{f}3k})^2} \tag{11}$$

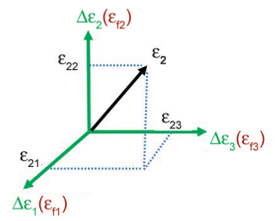

Figure 3. The illustration for the determination of the effective strain.

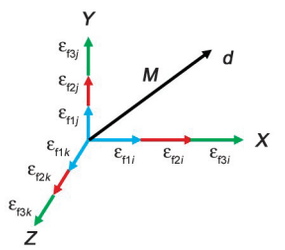

Figure 4. The illustration for the direction of the effective strain.

The illustration for the direction of the effective strain is shown in Figure 4.

3. Fatigue experiment and finite element models of the ring specimen

A type of a ring specimen, made from natural rubber and steel, was used for fatigue tests by Mars and Fatemi [13, 24]. The specimen, a rubber layer bounded by a top and a bottom metal plate, had approximately 76 mm in inner diameter and approximately 11 mm in height. Figure 5 shows the specimen with loading indication. The details of the specimen can be found in reference [24]. 15 types of fatigue loading paths (90 fatigue cases) with different R ratios (ratio between the minimum and maximum load), preloads, and phase angles, named from Path A to O, were applied in the experiments. $R = 0$ means that the minimum load is 0, and $R = -1$ means that the minimum load is in the opposite direction against the maximum load with the same magnitude. For simplicity, all loading paths were classified into four Groups:
Group A – tension
Group B – torsion
Group C – tension + torsion in phase
Group D – tension + torsion out of phase.
Three finite element models for the ring specimen were created: two axisymmetric model with CGAX4RH [25] elements and one solid three-dimensional model with C3D8RH elements. The

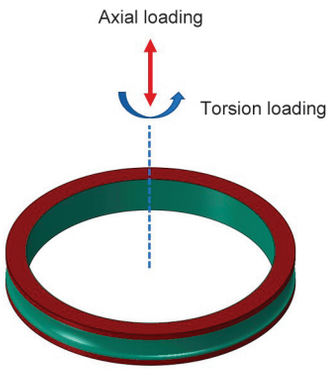

Figure 5. The ring specimen: Red for metal and blue for rubber.

CGAX4RH elements are a type of twist elements with 4-node bilinear, reduced integration with hourglass control, and hybrid with constant pressure. The C3D8RH elements are a type of solid elements with 8-node linear brick, reduced integration with hourglass control, and hybrid with constant pressure. A reference point was set up to control the top surface/edge. The bottom surface/edge was fixed. An external loading was applied to the reference point directly. To test mesh sensitivity, one axisymmetric model with mesh size 0.3 mm, shown in Figure 6a, and one axisymmetric model with mesh size 0.6 mm, shown in Figure 6b, were utilised. The maximum tensile displacement 9.9 mm in Group A was taken as the benchmark loading case. Figure 6c and 6d illustrate the maximum strain results for both the models where the strain 99.99% was for the model with 0.3 mm mesh and the strain 98.34% was for the model with 0.6 mm mesh. The difference was 1.68% between the two models. Hence, the model with 0.3 mm mesh was used to calculate the fatigue damage. A solid three-dimensional model with a mesh size 0.6 mm was generated and used for the failure plane calculations, as shown in Figure 6e. The total degrees of freedom were approximately 2800 for the axisymmetric model with a mesh size 0.3 mm and approximately 510 000 for the solid model.

4. Verification of fatigue criterion and discussions

4.1. Constitutive material model and its validation

A general form of classic hyperelastic models [25–28] can be written as Equation (12):

$$W = W_{\mathrm{I}}(\bar{I}) + W_{\mathrm{J}}(J) \tag{12}$$

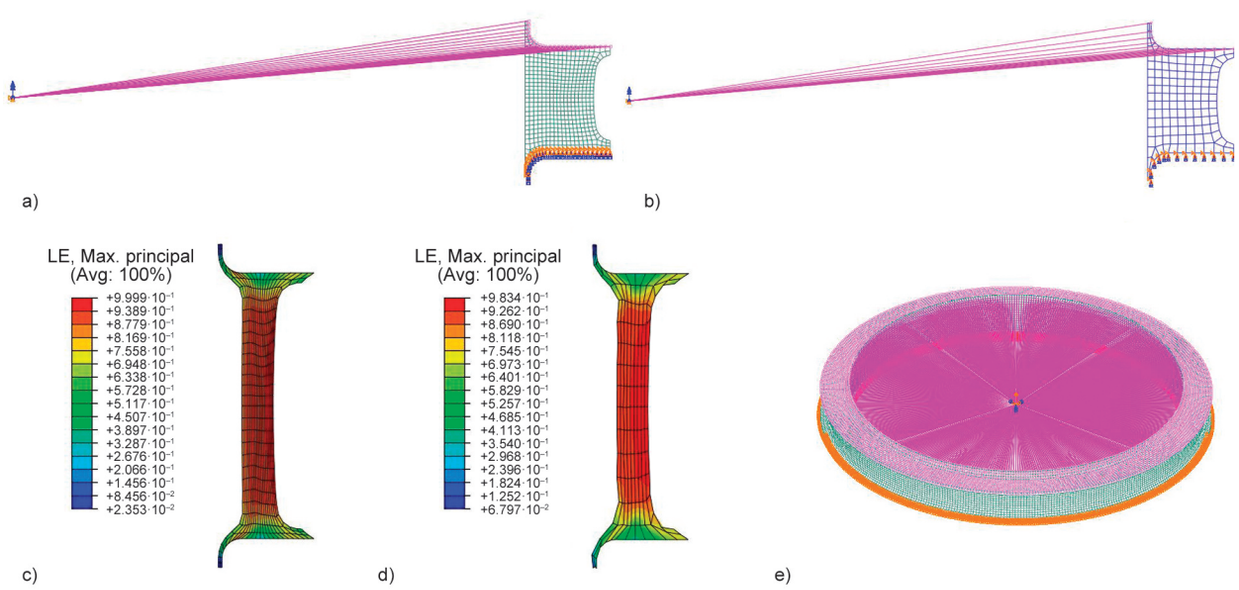

Figure 6. The finite element models of the ring specimen and the maximum strain comparison between the two models under the axial loading. (a) Finite element model with mesh size 0.3 mm: the bottom edge was fixed, and the loadings were applied on the top edge via a control point. (b) Finite element model with mesh size 0.6 mm: the bottom edge was fixed, and the loadings were applied on the top edge via a control point. (c) The maximum principal strain in the Finite element model with mesh size 0.3 mm, the axial loading 0–9.9 mm. (d) The maximum principal strain in the Finite element model with mesh size 0.6 mm, the axial loading 0–9.9mm. (e) Three-dimensional finite element model: the bottom surface was fixed, and the loadings were applied on the top surface through a control point.

where $W_I(\bar{I})$ is the deviatoric part of the strain energy density of the primary material response; $W_J(J)$ is the volumetric part of the strain energy density.
$\bar{I}$ can be further expanded to $\bar{I}_1$ and $\bar{I}_2$, which are an alternative set of the invariants of the Left Cauchy-Green deformation tensor **b** (Equations (13)–(16):

$$\bar{I}_1 = \frac{I_1}{J^{\frac{2}{3}}} \tag{13}$$

$$\bar{I}_2 = \frac{I_2}{J^{\frac{4}{3}}} \tag{14}$$

$$I_1 = \mathrm{trace}(\mathbf{b}) \tag{15}$$

$$I_2 = \frac{1}{2}\left(I_1^2 - \mathbf{b}\cdot\mathbf{b}\right) \tag{16}$$

The left Cauchy-green deformation tensor **b** can be expressed using the deformation gradient tensor **F** (Equation (17)–(19)):

$$\mathbf{F} = \begin{Bmatrix} 1+\frac{\partial u_1}{\partial x_1} & \frac{\partial u_1}{\partial x_2} & \frac{\partial u_1}{\partial x_3} \\ \frac{\partial u_2}{\partial x_1} & 1+\frac{\partial u_2}{\partial x_2} & \frac{\partial u_2}{\partial x_3} \\ \frac{\partial u_3}{\partial x_1} & \frac{\partial u_3}{\partial x_2} & 1+\frac{\partial u_3}{\partial x_3} \end{Bmatrix} \tag{17}$$

or

$$F_{ij} = \delta_{ij} + \frac{\partial u_i}{\partial x_j} \tag{18}$$

$$\mathbf{b} = \mathbf{F}\cdot\mathbf{F}^{\mathbf{T}},, \quad b_{ij} = F_{ik}F_{jk} \tag{19}$$

J is the Jacobian of the deformation gradient and a measure of the volume change caused by a deformation (Equation (20)):

$$J = \sqrt{\det(\mathbf{b})} = \det(\mathbf{F}) \tag{20}$$

The stress-strain law can be obtained by differentiating the strain energy density and the results are given below (Equation (21), (22)):

$$\sigma_{ij} = \frac{2}{J}\left[\frac{1}{J^{\frac{2}{3}}}\left(\frac{\partial W}{\partial \bar{I}_1} + \bar{I}_1\frac{\partial W}{\partial \bar{I}_2}\right)b_{ij} - \left(\bar{I}_1\frac{\partial W}{\partial \bar{I}_1} + 2\bar{I}_2\frac{\partial W}{\partial \bar{I}_2}\right)\frac{\delta_{ij}}{3} - \frac{1}{J^{\frac{4}{3}}}\frac{\partial W}{\partial \bar{I}_2}b_{ik}b_{kj}\right] + \frac{\partial W}{\partial J}\delta_{ij} \tag{21}$$

where δ_{ij} is the Kronecker delta.
A form of polynomial ($N = 2$) was used to model this ring specimen and to predict the fatigue damage:

$$W = C_{10}(\bar{I}_1 - 3) + C_{01}(\bar{I}_2 - 3) + C_{20}(\bar{I}_1 - 3)^2 + C_{11}(\bar{I}_1 - 3)(\bar{I}_2 - 3) + C_{02}(\bar{I}_2 - 3)^2 + \frac{1}{D_1}(J-1)^2 + \frac{1}{D_2}(J-1)^4 \tag{22}$$

where C_{ij} and D_i are constants.
The constitutive model used is a strain rate independent phenomenological model. The response of a real rubber depends strongly on the strain rate, the excitation frequency, and the temperature. From reference [24], the test frequencies ranged between 0.5 and 4 Hz (except for one test at 6 Hz), with the higher frequencies at smaller amplitudes (longer lives), to avoid any significant cyclic heating. Hence, in such quasi-static conditions, it would be suitable to use Equation (22) for the fatigue evaluation.
The material constants were obtained from the experimental data in compression, tension, plane shear, and volumetric tests. The constants were then used to test industrial products to validate their accuracy. Finally, the verified constants were input into the company's database. The parameters of the material model are listed in Table 1. D_1 and D_2 represent the compressibility of rubber materials. These constants have been verified through the load-deflection response from an uncontained condition to a nearly contained condition using industrial products. A typical engineering case is presented in [29] using this value. We suggest that the compressibility should be included in the model to avoid a small but not negligible effect in uncontained loading cases. The value given could provide a reference for the readers.
The stability of the material model (Drucker-stability) was performed for nominal strain values (change in length per unit of original length). The results were: unstable at a nominal strain larger than 200% for uniaxial tension; unstable at a nominal strain less than –79% for uniaxial compression; unstable at a nominal strain larger than 116% for biaxial tension; unstable at a nominal strain less than –42% for biaxial compression; stable for all strains for planar tension, planar compression, volumetric tension, volumetric compression, and all volume ratios.
To verify the suitability of the material model, two response curves, one in tension and the other in torsion, were calculated. The predicted results were plotted in

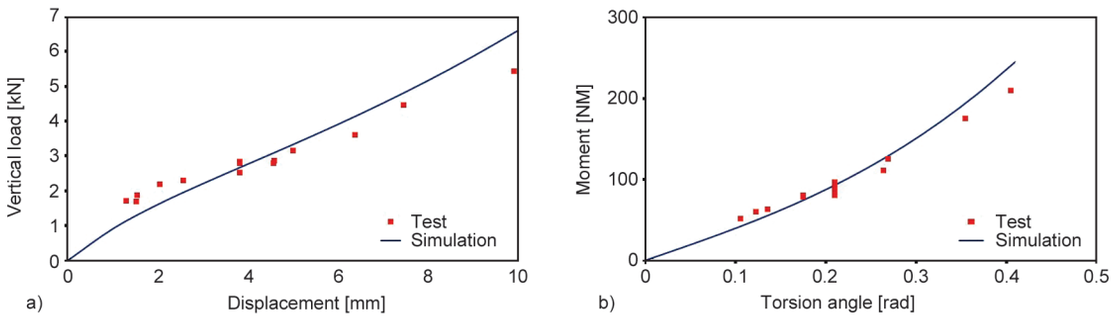

Figure 7. The comparison of the load-deflection curves. (a) Load-deflection curve under tension. (b) Load-deflection curve under torsion.

Table 1. Hyperelastic constants: $N = 2$.

C_{10} [MPa]	C_{01} [MPa]	C_{20} [MPa]	C_{11} [MPa]	C_{02} [MPa]	$D_1 = D_2$ [MPa^{-1}]
0.439	0.212	0.097	-0.0907	0.0372	0.008

Figure 7. The coefficient of determination was $R^2 = 0.88$ for Figure 7a and $R^2 = 0.95$ for Figure 7b, which seemed to be consistent with the test data. Since the exact strain rate was not available, these values can only be taken as a good indication. Hence, the selected model fitted the load-deflection response (even if the exact strain rate is unknown). This form of the strain energy density was utilised to verify the fatigue damage criterion.

4.2. Fatigue damage prediction

The proposed damage criterion was applied to the four groups. Detailed calculation is described below.

Group A:

It contained 14 tension cases under $R = 0$ condition in reference [24] Path A: loading range from 0~1.27 to 0.01~9.90 mm). The maximum effective strain occurred in the middle of the outside surface on which the fatigue cracks were observed. Figure 8a illustrates the effective strain profile in one case: 0~7.44 mm along the vertical direction.

Group B:

It consisted of 31 torsion cases in reference [24]: $R = 0$ and $R = -1$, with and without preload (Path B: loading ranges from 0~6 to 0~23.2°; Path C: loading ranges from –5.4~5.4 to –15~15°; Path J preloads in compression: -9~9 to –14.8~14.6°; Path K preloads in tension: –8~8 to –12~12°; Path M without preloads: –7~7 to –15~15°). Figure 8b shows an effective strain profile in a typical case: 0~10° torsion. The locations of the maximum effective strain were also consistent with the experimental observations.

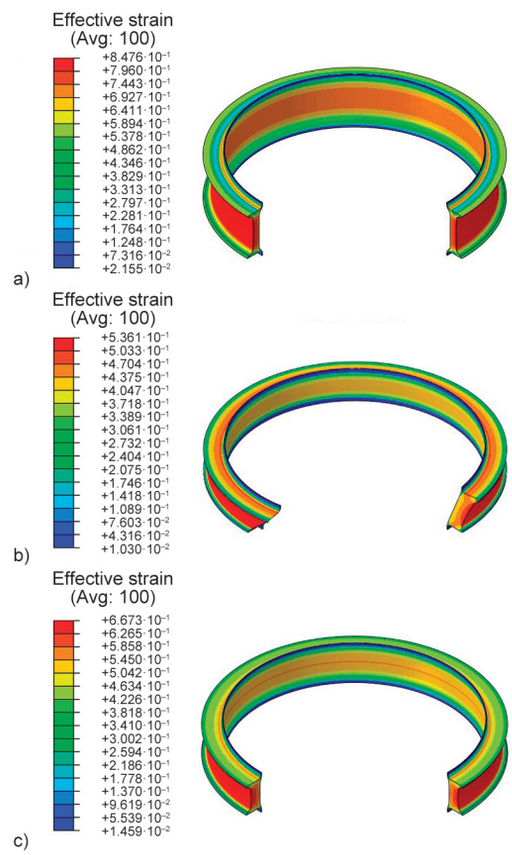

Figure 8. Sample cases for proportional loading cases. (a) Effective strain at displacement range 0–7.44 mm in Group A. (b) Effective strain at torsion angle range 0–10° in Group B. (c) Effective strain at displacement 2.54 mm and torsion angle 10° in Group C.

Group C:

It comprised 26 combined axial displacement and torsion cases in phase with $R = 0$ and $R = -1$ in reference [24]: (Path D: from 0~0.76 to 0~5.01 mm in displacement and 0~3 to 0~20° in angle; Path E: from –0.74~0.76 to –2.03~2.03 mm in displacement and –3~3 to –8~8° in angle; Path F: from –0.01~1,51

to 0~1.52 mm in displacement and 0~12 to 0~20° in angle; Path N: from –0.08~1.36 to –0.09~3.13 mm in displacement and 0~5.9 to 0~13.6° in angle). Figure 8c displays a profile of the effective strain at tension 2.54 mm and torsion 10°. The fatigue cracks appeared around the places where the maximum effective strain was located.

Group D:

It comprised 19 combined tension(compression)-torsion cases out of phase in reference [24] (Path G in a phase angle 45°: from –0.01~1.51 to 0~1.52 mm in displacement and 0~12 to 0~20° in angle; Path H in a phase angle 90°: from 0~0.76 to –0.01~3.52 mm in displacement and 0~3 to 0~14.1° in angle; Path I in a phase angle 180°: from 0~0.76 to –0.01~3.52 mm in displacement and 0~3 to 0~14.1° in angle; Path L in a phase angle 180°: from 0~–0.76 to 0~–1.52 mm in displacement and 0~10 to 0~20° in angle; Path O in a phase angle 90°: from –0.05~1.33 to 0.2~4.27 mm in displacement and 0~5.4 to 0~13.2° in angle.). Unlike a proportional loading, it is much more complex in a non-proportional loading. To find the critical effective strain in a loading cycle, a calculation procedure needs to be performed at different loading proportions with varying bases over one complete loading cycle to obtain effective strain histories. A base is a starting point to calculate the fatigue loading range. Since the base is changed, the corresponding loading proportion in the total loading range is also changed. This procedure can be called moving base method, *i.e.*, the starting base is not fixed. For example, a cyclic loading procedure is in a range from 1 to 10 kN, a moving base can be started from 2, 3, and 4 kN *et al.* and corresponding ranges are 8, 7, and 6 kN *et al.* The critical plane method is effective under a fixed loading range. Under a non-proportional loading procedure, a range that generates the maximum damage is unknown. Hence, substantial calculation time is needed to find different damage values over different loading ranges using the critical plane method.

Figure 9a illustrates two events with the same maximum loading value 1 and a phase angle 90°. One completed loading cycle was divided into 4 sectors. For safety, it is suggested to include more sectors to calculate the maximum damage. One sector is further divided into 10 portions, as shown in Figure 9b. Applying the moving base method, the maximum damage in each loading range can be found. It is

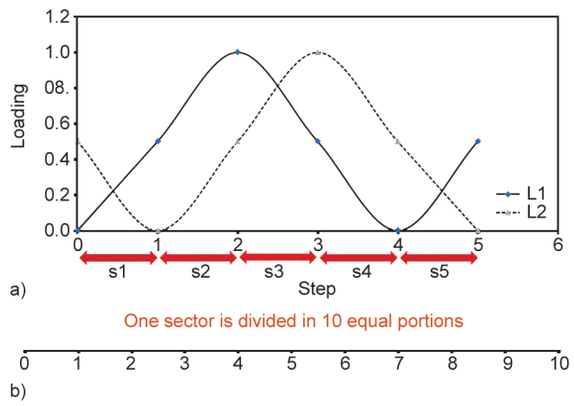

Figure 9. The sectors and the portions in a loading procedure. (a) One complete cycle is divided into 4 sectors. (b) One sector is divided in 10 equal portions.

important to calculate the effective strain over at least one loading cycle. Finally, the highest values in each loading range were compared, and the critical loading range was determined. For the critical plane method, this process would involve a great amount of calculation work to obtain the fatigue damage values for each rotated potential failure plane over every calculated range. Therefore, the proposed effective strain method would reduce the significant calculation time compared with the critical plane method.

A fatigue loading case with displacement range 0–2.54 mm and torsion range from 0–10° at a phase angle 45° was taken for demonstration. Figure 10 illustrates an effective strain history against the axial displacement from 0–2.54 mm and against the torsion angle from 0–10°, respectively, where the highest value of the effective strain was 46% based on counting from the displacement 0. Figure 11 shows the same loading range, where the highest value of the effective strain was 57% based on counting from the torsion angle 0. A comparison was made from the values of Figure 10 and 11 as well as the others in different loading ranges. It was found that 57% was the maximum effective strain over this load range, *i.e.*, starting from torsion angle 0. Figure 12 shows the profile of the maximum effective strain that matched the experimental observation. In fact, from Figure 10 and 11, the response between the points in each sector varied monodirectionally and smoothly. This observation indicated that the maximum value could be located at a range between both ends of the sectors.

Furthermore, a more severe out-of-phase case with a phase angle 90° was investigated based on the

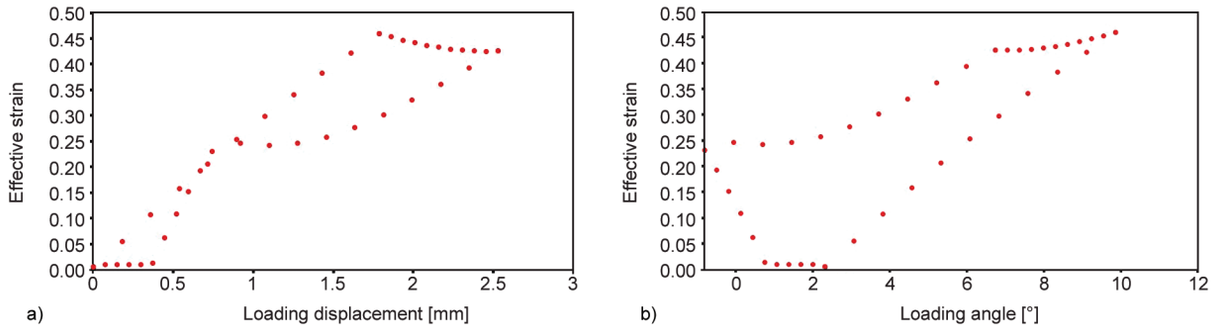

Figure 10. Effective strain history from a displacement range 0–2.54 mm and a torsion angle range from 0–10° at a phase angle 45° in group D, starting from 0 displacement. (a) Effective strain against loading displacement. (b) Effective strain against loading angle.

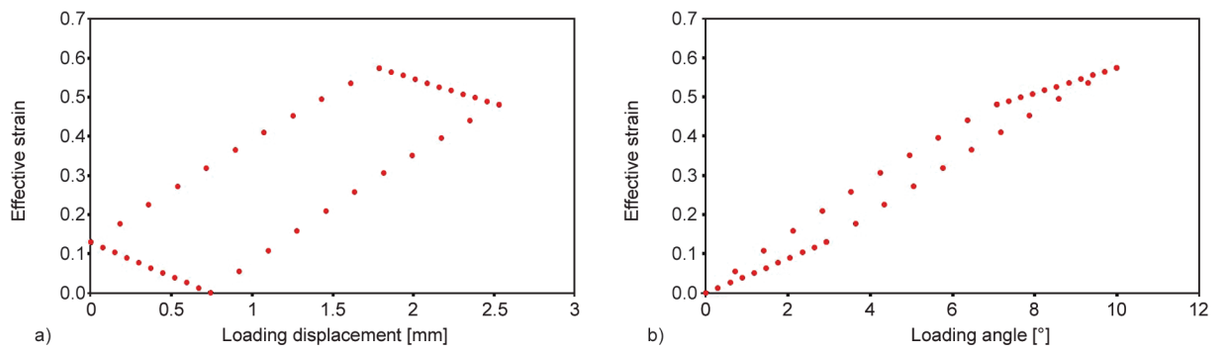

Figure 11. Effective strain history from a displacement range 0–2.54 mm and a torsion angle range from 0–10° at a phase angle 45° in group D, starting from 0 torsion. (a) Effective strain against loading displacement. (b) Effective strain against loading angle.

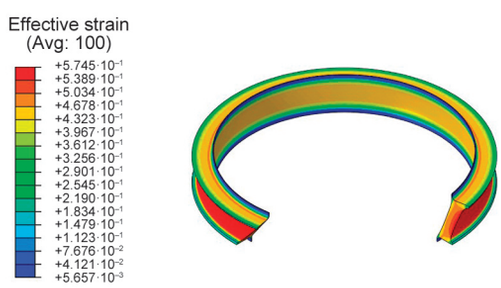

Figure 12. A sample case for non-proportional loading: the maximum effective strain profile at a displacement range 0–2.54 mm and a torsion angle range from 0–10° at a phase angle 45° in group D.

same procedure in the case with the phase angle of 45°. This loading case had a displacement range 0–0.76 mm and torsion angle range from 0–3°. An effective strain history against the axial displacement from 0–0.76 mm and against the torsion angle from 0–3°, respectively, as shown in Figure 13 where the highest value of the effective strain was 13% based on the range counting from the displacement 0. Figure 14 shows the same loading range, where the highest value of the effective strain was 17% based on the counting from the torsion angle 0. A comparison was made from other moving bases, and it was found that 17% was the maximum value under this loading case, as shown in Figure 15. The failure places were located on the outer surface of the specimen, where the crack was found from the experimental observation.

A direct comparison was made for the two non-proportional cases. For the case with the phase angle 45°, there was 24% difference between the maximum damage and the damage generated from the load range starting from displacement 0. For the case with the phase angle of 90°, the difference reached 31%. In the critical plane method, the maximum damage is obtained by rotating a predefined plane at a fixed angle and comparing the damage value in each plane. If a typical 15° angle is used for a three-dimensional case, it would need 1728 calculations for each integration point in all of the elements. The significant CPU time would be needed to obtain the same accuracy as that from this effective strain approach since the maximum damage can be obtained directly using Equation (2). However, this proposed approach is not intended to replace the critical plane method. Instead, it would be possible to combine the

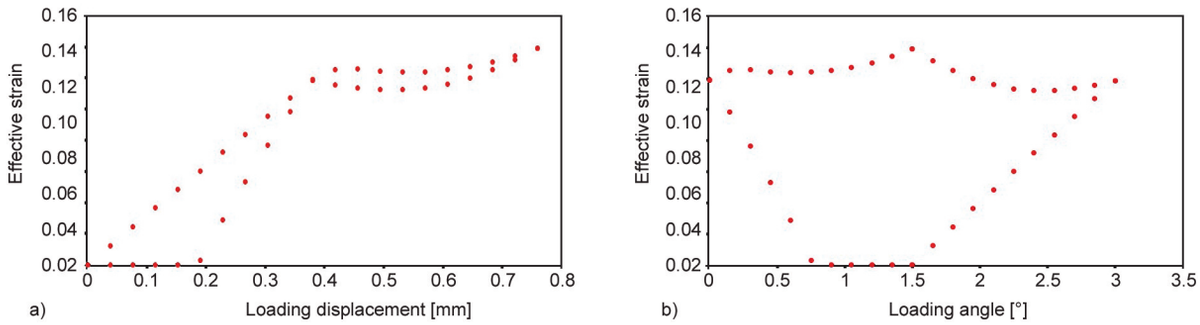

Figure 13. Effective strain history from displacement range 0–0.76 mm and torsion angle range from 0–3° at a phase angle 90° in group D, starting from 0 displacement. (a) Effective strain against loading displacement. (b) Effective strain against loading angle.

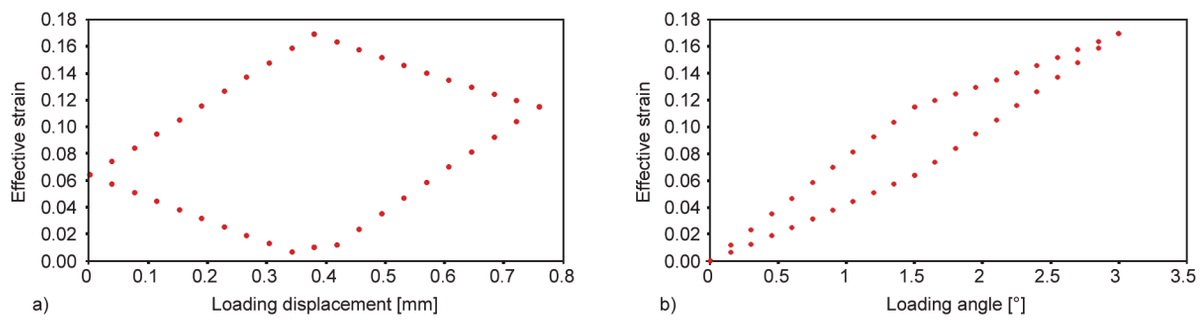

Figure 14. Effective strain history from displacement range 0–0.76 mm and torsion angle range from 0–3° at a phase angle 90° in group D, starting from 0 torsion. (a) Effective strain against loading displacement. (b) Effective strain against loading angle. (a) Effective strain against loading displacement. (b) Effective strain against loading angle.

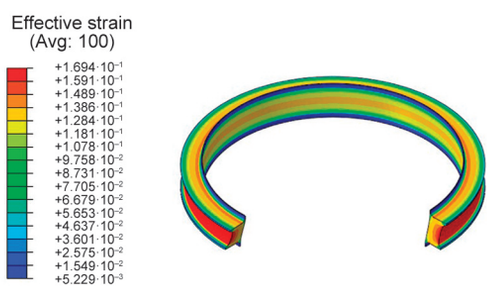

Figure 15. A further non-proportional case: the maximum effective strain profile under the loading case: the displacement range 0–0.76 mm and the torsion angle range 0–3° at a phase angle 90° in group D.

two approaches together, *i.e.*, finding the critical loading range using the proposed approach first and then applying the critical plane method for this loading range to obtain the maximum damage.

4.3. Failure plane prediction

The magnitude (Equations (2)) of the effective strain is associated with fatigue damage, whereas its direction (Equations (6)–(11)) is related to the failure plane. Instead of using the critical plane method, the analytical Equations (6)–(11) can be directly employed to calculate the orientation of the effective strain, from which the direction of the failure plane can be obtained. The following outcomes were compared with the experimental results available to verify the failure plane calculated from the proposed effective strain criterion.

For Group A:

The calculated direction of all the cracks was all in the horizontal plane, *i.e.*, the angles of the cracks were 0°, as indicated in Figure 16a. The actual orientation of the cracks observed was the same as the calculated ones.

For Group B:

Calculations of the failure planes were performed on the cases $R = -1$ without preloading. The calculated direction was in the range of –43.1 to –47.2°, as shown in Figure 16b. The observed angles of these cases were –45°. By reversing the torsion direction, the calculated angles were between 43.1 to 47.2°, which were against the observed angle of 45°.

There is a correlation between the crack angle and the loading angle. Figure 16c illustrates the relationship between the crack angle in the deformed states and the loading angles. The regression analysis indicated nearly a linear correlation with the statistical

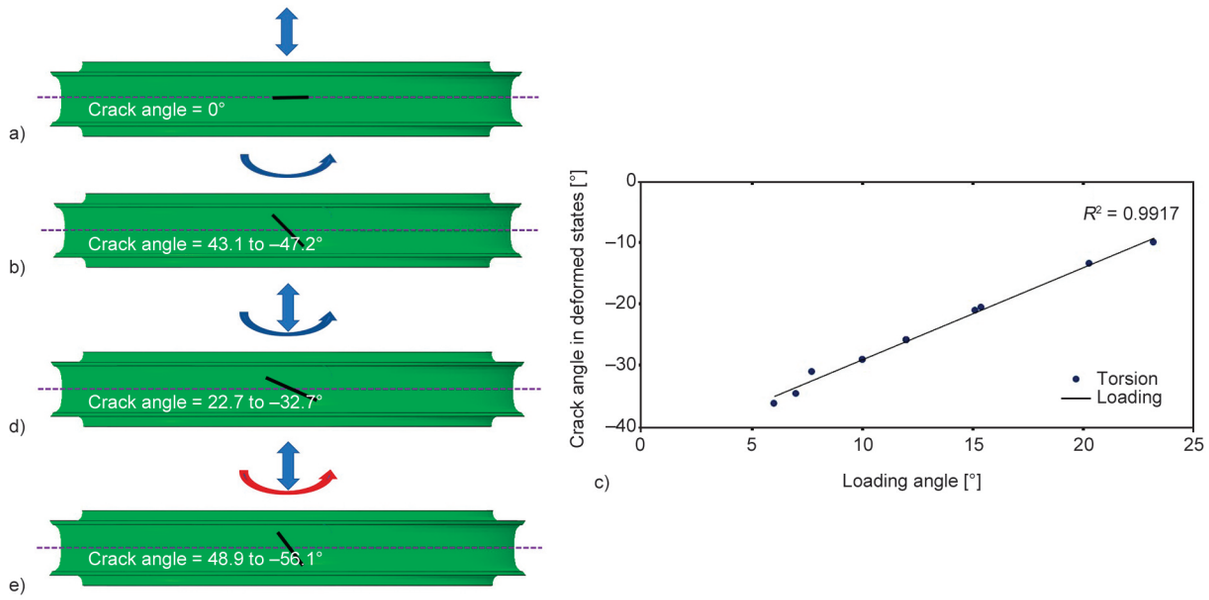

Figure 16. Predicted crack orientation. (a) Crack indication in Group A: tension loading. (b) Crack indication in Group B: torsion loading – $R = -1$ with axial displacement = 0. (c) The relationship between the applied loading angles and the crack angles under the deformed states. (d) Crack indication in Group C: tension + torsion loading in phase with $R = -1$. (e) Crack indication in Group D: tension + torsion loading with a phase angle = 45°.

measure $R^2 = 0.9917$. Hence, from the effective strain criterion, the larger the loading angle, the smaller the crack angle in a deformed state.

For Group C:
The cases with $R = -1$ were investigated. The calculated directions of the cracks were in the range of -22.7 to –32.7°, as illustrated in Figure 16d. The angles of the cracks from the experimental observation were in the range of -25 to -30°.

For Group D:
Calculations on the cases with phase angle 45° were carried out. The calculated directions of the cracks were in the range of –48.9 to –56.1°, as displayed in Figure 16e. The range of –40 to –55° was observed experimentally.
The above angle comparisons are summarised in Table 2.

4.4. A unified for all fatigue load cases

From Section 4.2, it was demonstrated that real fatigue cracks appeared at the locations where the effective strain reached its maximum. From Section 4.3, it was verified that the failure planes predicted were consistent with the experimental observations. Hence, a unified for all fatigue loading cases was generated so that the final verification could be established and the fatigue damage of similar rubber material could be evaluated. Figure 17 illustrates an S–N curve for all 90 fatigue loading cases investigated. The coefficient of determination R^2 was 0.71,

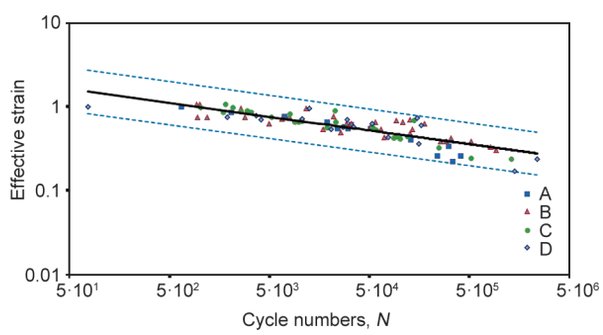

Figure 17. The S–N curve with a scatter factor of 1.6 for all 90 fatigue loading cases: A – tension; B – torsion; C– tension + torsion in phase; D – tension + torsion out of phase.

Table 2. Crack orientation comparison between the observation and the prediction on selected fatigue cases.

Group	Experimental observation [°]	Prediction [°]	Note
A	0	0	All fatigue cases.
B	–45 45	–43.1 to –47.2 43.1 to 47.2	$R = -1$ without pre-loading.
C	–25 to –30	–22.7 to –32.7	$R = -1$.
D	–40 to –55	–48.9 to –56.1	$R = 0$, phase angle = 45°.

and the scatter band of 1.6 was achieved for the effective strain ε_f against the cycle numbers. The expression of the S–N curve was (Equation (23)):

$$\varepsilon_f = 3.064N^{-0.164} \tag{23}$$

5. Conclusions

The effective strain criterion was proposed and applied to the rubber ring specimens utilised in the fatigue experiments in multimode and multiaxial loading conditions [13, 24]. These test data consisted of 4 groups with 90 fatigue cases. The validation procedure was performed in two aspects: fatigue damage and crack orientation.

The main findings from the investigation are listed below:

1. All predicted fatigue cracks were on the outer surface of the ring where the effective strain reached its maximum and was consistent with experimental observation.
2. It was demonstrated that the failure planes predicted correlated well with the experimental measurements in each group.
3. The obtained S-N curve, generated from 90 fatigue cases and covered over 10^2 to $2.4 \cdot 10^6$ cycles, achieved high accuracy with a scatter-band of 1.6.
4. The CPU time, compared with the critical plane method, would be reduced significantly for fatigue evaluation as both the damage and the crack orientation can be calculated using analytical expressions.
5. The proposed approach was applied to two non-proportional loading cases (one in phase angle 45° and the other in phase angle 90°). The results seemed to indicate the suitability of the approach for the non-proportional loading calculations. It would be possible to combine the proposed approach with the critical plane method in non-proportional loadings: using the proposed approach to find the critical loading range and then using the critical plane method to find the maximum values of the required damage variables. Both the proposed concept and the obtained S–N curve would be beneficial in rubber fatigue design in the industry.
6. It would be difficult to calculate fatigue damage in all possible conditions in one investigation. Further research may be needed to study more cases and to compare the results with the literatures available, *e.g.*, reference [30–32]. The author would like to report the progress in due course.

References

[1] Bourchak M., Aid A.: PE-HD fatigue damage accumulation under variable loading based on various damage models. Express Polymer Letters, **11**, 117–126 (2017). https://doi.org/10.3144/expresspolymlett.2017.13

[2] Verron E.: Prediction of fatigue crack initiation in rubber with the help of configurational mechanics. in 'Constitutive models for rubber IV' (eds.: Austrell P., Kari L.) A. A. Balkema Publishers, Leiden, 3–8 (2005).

[3] le Cam J-B., Huneau B., Verron E.: Fatigue damage in carbon black filled natural rubber under uni- and multiaxial loading conditions. International Journal of Fatigue, **52**, 82–94 (2013). https://doi.org/10.1016/j.ijfatigue.2013.02.022

[4] Luo R. K., Wu W. X., Cook P. W., Mortel W. J.: An approach to evaluate the service life of rubber springs used in rail vehicle suspensions. Journal of Rail and Rapid Transit, **218**, 173–177 (2004). https://doi.org/10.1243/0954409041319597

[5] Luo R. K., Wu W. X.: Fatigue failure analysis of anti-vibration rubber spring. Engineering Failure Analysis, **13**, 110–116 (2006). https://doi.org/10.1016/j.engfailanal.2004.10.012

[6] Wu W., Cook P., Luo R., Mortel W.: Fatigue life investigation in the design process of metacone rubber springs. Chapter 14 in 'Elastomers and components' (ed.: Coveney V.) Woodhead, Cambridge, 195–207 (2006). https://doi.org/10.1533/9781845691134.2.195

[7] Samad M. S. A., Aidy A., Sidhu R. S.: Durability of automotive jounce bumper. Materials and Design, **32**, 1001–1005 (2011). https://doi.org/10.1016/j.matdes.2010.08.017

[8] Luo R. K.: Effective stress criterion for rubber multiaxial fatigue under both proportional and non-proportional loadings. Engineering Failure Analysis, **121**, 105172 (2021). https://doi.org/10.1016/j.engfailanal.2020.105172

[9] Luo R. K.: Multiaxial fatigue prediction on crack initiation for rubber antivibration design – Location and orientation with stress ranges. Journal of Materials: Design and Applications, **235**, 469–480 (2021). https://doi.org/10.1177/1464420720969857

[10] Saintier N., Cailletaud G., Piques R.: Multiaxial fatigue life prediction for a natural rubber. International Journal of Fatigue, **28**, 530–539 (2006). https://doi.org/10.1016/j.ijfatigue.2005.05.011

[11] Mars W. V.: Multiaxial fatigue crack initiation in rubber. Tire Science and Technology, **29**, 171–185 (2001). https://doi.org/10.2346/1.2135237

[12] Mars W. V., Kingston J. G. R., Muhr A., Martin S., Wong K. W.: Fatigue life analysis of an exhaust mount. in 'Constitutive models for rubber IV' (eds.: Austrell P-E., Kari L.) A. A. Balkema Publishers, Leiden, 23–29 (2005).

[13] Mars W. V., Fatemi A.: Nucleation and growth of small fatigue cracks in filled natural rubber under multiaxial loading. Journal of Material Science, **41**, 7324–7332 (2006). https://doi.org/10.1007/s10853-006-0962-2

[14] Xu X., Zhou X., Liu Y.: Fatigue life prediction of rubber-sleeved stud shear connectors under shear load based on finite element simulation. Engineering Structures, **227**, 111449 (2021). https://doi.org/10.1016/j.engstruct.2020.111449

[15] Zarrin-Ghalami T., Datta S., Keinti R. B., Chandrashekar R.: Elastomeric component fatigue analysis: Rubber fatigue prediction and correlation comparing crack initiation and crack growth methodologies. SAE International Journal of Advances and Current Practice in Mobility, **2**, 1754–1763 (2020). https://doi.org/10.4271/2020-01-0193

[16] Zerrin-Ghalami T., Fatemi A.: Material deformation and fatigue behavior characterization for elastomeric component life predictions. Polymer Engineering and Science, **52**, 1795–1805 (2012). https://doi.org/10.1002/pen.23125

[17] Belkhiria S., Hamdi A., Fathallah R.: Strain-based criterion for uniaxial fatigue life prediction for an SBR rubber: Comparative study and development. Proceedings of the Institution of Mechanical Engineers, Part L: Journal of Materials: Design and Applications., **234**, 897–909 (2020). https://doi.org/10.1177/1464420720913595

[18] Zerrin-Ghalami T., Fatemi A.: Fatigue life predictions of rubber components: Applications to an automobile cradle mount. Proceedings of the Institution of Mechanical Engineers Part D: Journal of Automobile Engineering, **227**, 691–703 (2013). https://doi.org/10.1177/0954407012461863

[19] Shangguan W. B., Duan X., Liu T., Wang X., Zheng G., Yu B.: Study on the effect of different damage parameters on the predicting fatigue life of rubber isolators. Journal of Mechanical Engineering, **52**, 116–126 (2016). https://doi.org/10.3901/JME.2016.02.116

[20] Shangguan W-B., Zheng G-F., Liu T-K., Duan X-C., Rakheja S.: Prediction of fatigue life of rubber mounts using stress-based damage indexes. Journal of Materials: Design and Applications, **231**, 657–673 (2017). https://doi.org/10.1177/1464420715608407

[21] Nyaaba W., Bolarinwa E. O., Frimpong S.: Durability prediction of an ultra-large mining truck tire using an enhanced finite element method. Journal of Automobile Engineering, **233**, 161–169 (2019). https://doi.org/10.1177/0954407018795278

[22] Chung J., Kim N. H.: Numerical methods of multiaxial fatigue life prediction for elastomers under variable amplitude loadings. Fatigue and Fraction of Engineering Material and Structure, **39**, 866–876 (2016). https://doi.org/10.1111/ffe.12401

[23] Lu C., Melendez J., Martínez-Esnaola J. M.: Prediction of crack initiation plane direction in high-cycle multiaxial fatigue with in-phase and out-of-phase loading. Fatigue and Fracture of Engineering Materials and Structures, **40**, 1994–2007 (2017). https://doi.org/10.1111/ffe.12620

[24] Mars W. V., Fatemi A.: Multiaxial fatigue of rubber: Part II: Experimental observations and life predictions. Fatigue and Fracture of Engineering Materials and Structures, **28**, 523–538 (2005). https://doi.org/10.1111/j.1460-2695.2005.00895.x

[25] Dassault Systems: Abaqus user manual (2020).

[26] Ogden R. W.: Non-linear elastic deformations. Ellis Horwood, Chichester (1984).

[27] Bower A.: Applied mechanics of solids. CRC Press, Boca Raton (2010). https://doi.org/10.1201/9781439802489

[28] Luo R. K.: Simulation methods for rubber antivibration systems. World Scientific, Singapore (2020). https://doi.org/10.1142/11856

[29] Luo R. K.: Rubber fatigue evaluation for antivibration products and an S–N curve with a scatter band of 0.8. Proceedings of the Institution of Mechanical Engineers Part L: Journal of Materials: Design and Applications, **235**, 2382–2390 (2021). https://doi.org/10.1177/14644207211018238

[30] Klauke R., Alshuth T., Ihlemann J.: Lifetime prediction of rubber products under simple-shear loads with rotary axes. in 'Constitutive models for rubber VI' (eds.: Heinrich G., Kaliske M., Lion A., Reese S.) CRC Press, London, 235–240 (2009).

[31] Roberts B. J., Benzies J. B.: The relationship between uniaxial and equibiaxial fatigue in gum and carbon black filled vulcanizates. in 'Proceedings of Rubbercon77, Brighton, England' 2.1–2.13 (1977).

[32] Saintier N., Cailletaud G., Piques R.: Crack initiation and propagation under multiaxial fatigue in a natural rubber. International Journal of Fatigue, **28**, 61–72 (2006). https://doi.org/10.1016/j.ijfatigue.2005.03.006